Electrochemical and Solid-State Letters, **10** (10) K47-K49 (2007)
1099-0062/2007/10(10)/K47/3/$20.00 © The Electrochemical Society

Formation of Ferromagnetic Iron Core-Shell Nanocubes on a H-Terminated Si(100) Surface by Electrodeposition

L. Y. Zhao,[a] H. Jalili,[b] N. Panjwani,[a] T. Chan,[a] Z. H. He,[a] N. F. Heinig,[a] and K. T. Leung[a,b,z]

[a]*WATLab and Department of Chemistry, and* [b]*Department of Physics, University of Waterloo, Waterloo, Ontario, Canada N2L 3G1*

Near-monosized and uniformly distributed cubic Fe core-shell nanoparticles (with an average side length of 56 nm) were electrodeposited on H-terminated Si(100) in a $FeCl_2$ solution. X-ray photoelectron spectroscopy analysis indicates chemical states of the Fe nanocubes characteristic of predominant ferromagnetic metallic Fe cores covered by Fe_2O_3 shells. Glancing-incidence X-ray diffraction analysis reveals a body-centered cubic (bcc) lattice structure. A nanometer-thick film consisting of 2–3 layers of cuboidal nanoparticles of the same bcc Fe core and Fe_2O_3 shell can be obtained when the amount of charge transfer is increased. The prominent magnetic domains of these nanocubes can be illustrated by magnetic force microscopy.
 [DOI: 10.1149/1.2759604]

Manuscript submitted March 15, 2007; revised manuscript received June 3, 2007. Available electronically July 23, 2007.

Magnetic nanoparticles (NPs), particularly iron with its low-cost advantage, have attracted recent attention due to their potential applications in spin-based electronics,[1] data storage,[2] and targeted drug delivery.[3] Because NPs with different shapes should have different electronic, optical, magnetic, and catalytic properties,[4,5] various synthetic techniques have been developed to obtain iron NPs with different shapes and morphologies. In particular, near-spherical Fe NPs with diameters ranging from 6 to 35 nm were obtained by thermal evaporation and condensation of bulk metal in an inert atmosphere.[6] Metallic spherical Fe NPs, with an average height of 4–6 nm as determined by atomic force microscopy (AFM), were also obtained by first transferring ferritin molecules onto a SiO_2 support, and then followed by removal of the protein shells and reduction of the FeOOH NPs in hydrogen.[7] Moreover, arrays of cylindrical Fe NPs with a high aspect ratio (100–120 nm in length and 10 nm diameter) could be prepared with high precision by using a biased scanning tunneling microscopy (STM) tip to initiate chemical vapor deposition involving gaseous $Fe(CO)_5$.[8-10] Furthermore, amorphous Fe NPs with an average grain size of 5 nm were produced by electron beam deposition from an Fe_2O_3 source directly on a Si(100) substrate with and without an Al buffer layer.[11]

Among the various methods used to prepare nanoscale metal particles onto a substrate, electrochemical deposition offers a powerful attractive synthetic technique because not only is it a simple and inexpensive method but also the particle size, density, and distribution so produced could be easily controlled with high throughput by manipulating the deposition potential, current, and other parameters often at ambient temperature. Although individual nanostructured Fe nanodeposits have not been reported previously, there has been a considerable amount of studies on synthesizing Fe films onto different substrates by electrodeposition and more elaborate techniques including molecular beam epitaxy,[12] electron beam evaporation,[13] chemical vapor deposition,[14] sputtered deposition,[15] or thermal evaporation.[16] In the case of electrodeposition of Fe films, Lee et al. reported the growth of an α-Fe(110) film with homogeneous, nearly monosized nanostructures of spherical shapes on an n-type Si(111) substrate by pulsed electrodeposition in a nonaqueous solution.[17] Zarpellon et al. showed that the Fe film electrodeposited on a Si(111) substrate could have sub-μm grains with slightly flat terraces on the surface along with the presence of iron silicide.[18] When the Fe thin film was electrodeposited onto a Cu substrate, Matsushima et al. found that the surface morphology of the Fe film became more angular grainy.[19] Recently, we reported the synthesis of near-monosized Fe oval-shaped nanorods (130 nm length × 25 nm diameter), the so-called nanorice particles, and spherical NPs (6–40 nm diameter) by using electrodeposition on a H-Si(100) (i.e., H-terminated) electrode at different $FeCl_3$ concentrations.[20] Although these Fe core-shell NPs could be deposited with well-defined shapes uniformly, a considerable amount of oxide shell was found, which consequently limited the observable magnetic properties of the Fe core itself. To date, it remains a big challenge to deposit a homogeneous layer of individual, well-defined nanostructured particles with significant Fe cores. The controlled fabrication of such a layer of magnetic NPs, or patterns thereof, may have significant practical applications.

In the present work, we show that cubic Fe NPs with a considerably thinner passivating oxide layer (i.e., a significant Fe core) can be obtained by replacing the Fe(III) ions with Fe(II) ions in electrochemical deposition on a H-Si(100) surface (from an aqueous $FeCl_2$ solution). Unlike electroplating in which Fe is usually deposited as a film,[21] we demonstrate controlled electrodeposition of Fe in the form of discrete metallic NPs, and by increasing the amount of charge transfer a thin film consisting of cuboidal NPs of Fe can be obtained. The morphology of the cubic Fe NPs is determined by field-emission scanning electron microscopy (SEM), while the chemical states and bulk crystal structures of these Fe NPs are characterized by X-ray photoelectron spectroscopy (XPS) and glancing-incidence X-ray diffraction (GIXRD), respectively. The magnetic properties of these cubic Fe NPs with their large Fe cores are investigated by magnetic force microscopy (MFM). The prominent MFM features suggest the presence of sub-μm magnetic domains in the nanometer-thick film of these cuboidal Fe nanostructured deposits.

Experimental

Details of our electrodeposition experiment and the three-electrode cell setup have been discussed elsewhere.[20] Si(100) (p-type, 30 × 15 mm, 0.4 mm thick, 1.0–1.5 mΩ cm) substrate was cleaned using the RCA method, etched in aqueous HF (2%) solution to remove the native oxide layer, and rinsed with Millipore water.[22] The resulting H-Si(100) is flat and terminated with hydrides (SiH_n, $n = 1$, 2, or 3), and is found to be suitable for uniform deposition of nanoparticles. In a fresh deoxygenated aqueous solution of 10 mM $FeCl_2$ and 0.2 M H_3BO_3 (pH 3.6), Fe NPs were deposited on the H-Si(100) substrate by amperometry potentiostatically at −1.4 V (relative to the Ag/AgCl reference electrode). After the deposition, the Si substrate was thoroughly rinsed with Millipore water and dried in N_2. The surface morphology of the Fe nanodeposits was characterized by SEM. The corresponding chemical composition was analyzed by XPS with a monochromatic Al Kα X-ray source (1486.6 eV), and at a typical energy resolution of 0.4–0.5 eV full width at half-maximum. The binding energy scale was calibrated to that of the Si $2p_{3/2}$ photopeak of bulk Si (99.3 eV),[23] because of recent reports of changes in the C 1s binding energy posi-

[z] E-mail: tong@uwaterloo.ca

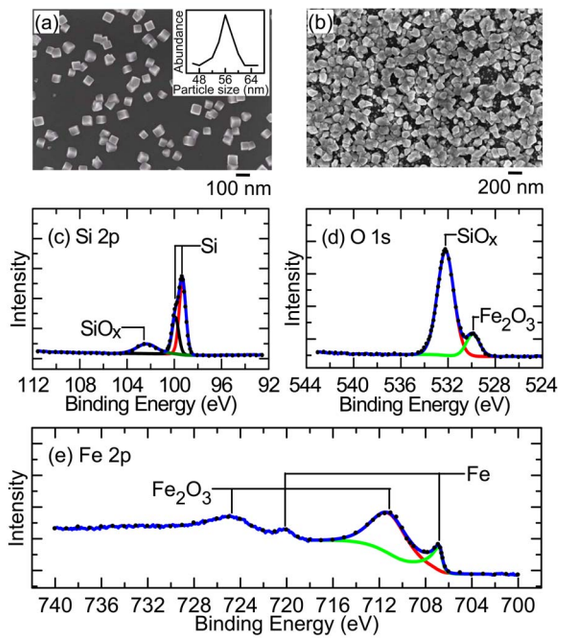

Figure 1. (Color online) SEM images of (a) Fe cubic nanoparticles and (b) a cuboidal nanostructured Fe film electrodeposited on H-terminated Si(100) at −1.4 V and 3.5 mC, and 70 mC, respectively; and the corresponding XPS spectra of (c) Si 2p, (d) O 1s, and (e) Fe 2p regions for the Fe nanocubes shown in (a). The experimental data (•) are fitted with, where appropriate, spin-orbit split states, and the fitted curves are shown as solid lines. The inset in (a) shows the relative abundance of the Fe cubic nanoparticles as a function of particle size.

tion of the residual carbon on different surfaces.[24] The structural characterization of the nanodeposits was determined by GIXRD at an incidence angle omega = 0.6°, with the Cu Kα anode operating at 45 kV and 40 mA. The divergent X-ray beam was collimated by a graded multilayer parabolic X-ray mirror, and the X-ray spot size on the sample surface was further defined by a 10 mm beam mask and a 1/16° divergence slit. For the MFM experiments, both the monolithic Si tips coated with hard-magnetic Co alloy and the sample were premagnetized by a neodymium magnet (with a residual flux density of 1.3 T).

Results and Discussion

Figure 1a shows the SEM micrograph of the as-deposited Fe NPs on a H-Si(100) substrate (at −1.4 V and 3.5 mC). Evidently, near-monosized cubic NPs with an average side length of 56 ± 5 nm were found to deposit uniformly on the Si substrate. When we first used the same electrolyte ($NaClO_4$ or KCl) as that used in our oval-shaped nanorod electrodeposition involving $FeCl_3$,[20] distorted cuboidal Fe NPs were found to always codeposit along with a Fe film. By changing the electrolyte to H_3BO_3, we were able to produce well-defined cubic Fe NPs exclusively, i.e., without the codeposited film, on the Si(100) substrate (Fig. 1a). The change in the pH value of the electrodeposition solution (from 5 to 3.6) could affect the nucleation and growth morphology of these Fe NPs. When the charge transfer was increased to 70 mC at a deposition potential fixed at −1.4 V, the consequent increase in the number of cubic Fe NPs evidently led to shape distortion and clustering, resulting in a nanostructured film of 2–3 layers of cuboidal NPs (all with a similar size of ~130 nm) on the H-Si(100) substrate. The SEM micrograph of one such typical film with an estimated thickness of 120 nm is shown in Fig. 1b. At a fixed total charge transfer, the growth of the NPs was also found to follow the general trend that the number density increases while the particle size decreases with increasing deposition voltage. The current transients were found to increase near linearly with the square root of the deposition time, which is characteristic of instantaneous nucleation and the island growth mode of deposition.[25] The electrodeposition of Fe NPs on Si(100) substrate in a solution of $FeCl_3$ (Ref. 20) or $FeCl_2$ therefore follows the instantaneous growth mechanism.

The corresponding XPS survey spectrum (not shown) for the cubic NPs reveals only contributions from Si, C, O, and Fe (and no other elements). In Fig. 1c, the two features at 99.3 and 99.9 eV correspond, respectively, to the Si $2p_{3/2}$ and $2p_{1/2}$ components of elemental Si (with the intensity ratio of 2:1 and a typical spin-orbit splitting of 0.6 eV),[26,27] while the weak broad feature at 102.4 eV can be attributed to Si 2p of silicon suboxide (SiO_x).[28,29] The presence of the latter SiO_x feature therefore indicates partial oxidation of the Si substrate, likely induced by the electrodeposition. The formation of SiO_x is also consistent with the strong characteristic O 1s feature at 532.2 eV, shown in Fig. 1d. The weak O 1s feature found at 529.9 eV can be attributed to Fe_2O_3.[30] In the Fe 2p region (Fig. 1e), the features at 706.8 eV (720.1 eV) and 711.1 eV (724.7 eV) are consistent with the characteristic Fe $2p_{3/2}$ ($2p_{1/2}$) states for metallic Fe and Fe_2O_3, respectively.[31] Both the O 1s and Fe 2p XPS data therefore indicate the presence of an Fe_2O_3 shell with metallic Fe as the core of the cubic NP. Even though we also performed XPS depth-profiling experiments (not shown), it was difficult to determine the contribution of the Fe core from these data because ion sputtering has been found to cause reduction of Fe oxides to metallic Fe.[32] However, using the attenuation theory,[33] we were able to estimate the thickness of the Fe_2O_3 shell to be 2.5 nm from the ratio of the intensities of the Fe $2p_{3/2}$ photolines of Fe and Fe_2O_3. In our recent work involving electrodeposition in an $FeCl_3$ solution, the as-deposited oval-shaped nanorod Fe particles were found to consist of Fe cores with composite FeOOH and FeO shells, while the spherical NPs correspond to Fe cores with composite Fe_2O_3 and FeO shells.[20] In the present cubic NP case, there is a sizable Fe 2p feature corresponding to metallic Fe before sputtering, which was not observed in the case of the oval-shaped nanorods and spherical NPs. This confirms that the oxide shell for the cubic NPs must be not only thinner than those of the oval-shaped nanorods and spherical NPs but also less than the escape depth of the Fe 2p photoelectron at 780 eV kinetic energy (~6 nm).[33] Conversely, the relative amount of the Fe core in the cubic NPs is larger than those for the oval-shaped nanorods and spherical NPs. The surface morphology and the chemical composition of the Fe electrodeposits can therefore be effectively controlled by manipulating the oxidation states of the Fe salts used in the electrodeposition.

Figure 2 shows the GIXRD patterns of the Si(100) substrate with and without the Fe nanodeposits. The features at 50–60° are found to be in good accord with the (311) plane of the p-Si(100) substrate reported in the literature.[34] All the remaining peaks found for the Fe NPs shown in Fig. 2a can be ascribed to the (110), (200), (211), (220), and (310) planes of the bcc lattice of Fe (JCPDS 06-0696). After taking into account the instrumental linewidth (deduced from the GIXRD pattern of commercial metallic Fe powders obtained separately under the same experimental conditions), we estimated the particle size to be ~57 nm by using the Scherrer equation (with the Scherrer constant of 0.9),[35] in excellent agreement with our SEM results (Fig. 1a). No evidence of Fe_2O_3 was found from the XRD data, which indicates that either the amount of Fe_2O_3 was insufficient to be detected by GIXRD or more likely the surface Fe_2O_3 species is amorphous. Together with our earlier work involving $FeCl_3$ solution,[20] we demonstrate that three types of Fe NPs with different shapes and compositions can be obtained by appropriate manipulation of the electrodeposition parameters, including different Fe salts and different electrolyte solutions. The oval shape of the nanorod nanostructure could be due to codeposition of FeOOH (formed by hydrolysis in an aqueous $FeCl_3$ solution) during electrodeposition. Because hydrolysis could not occur in $FeCl_2$ solution

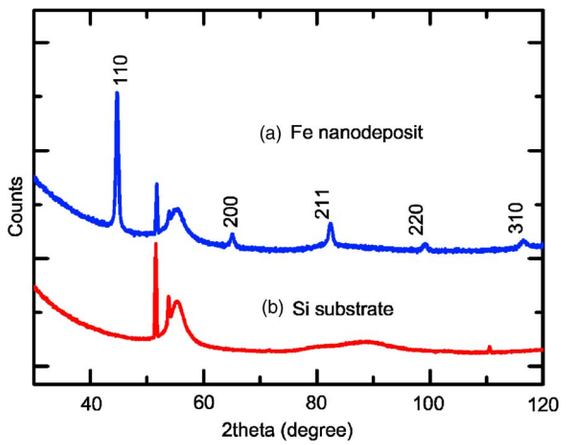

Figure 2. (Color online) GIXRD patterns of (a) Fe nanodeposits on H-terminated Si(100) and (b) a blank H-terminated Si(100) substrate, collected with an incidence angle omega = 0.6°.

and individual well-defined Fe NPs are probably single crystalline (bcc), the deposited metallic Fe NP could only be of cubic shape.

To illustrate the strong magnetic moments found in these Fe cuboidal NPs, we show in Fig. 3 AFM and MFM images of the Fe cuboidal nanoparticles deposited with the higher charge transfer 70 mC (Fig. 1b). The image correlation coefficient between the AFM and MFM images is found to be 0.0486, suggesting that the topography effect is negligible in the MFM image. Although the spatial distribution of the magnetic moments of individual NPs could form complicated patterns of magnetic interactions, the bright and dark regions of the observed MFM features are generally attributed to domains with magnetic moments pointing in opposite directions (i.e., upward and downward out of the sample plane). The presence of the extended magnetic domains with approximate segment widths of 0.5 μm and lengths of 1–3 μm is clearly found in the MFM image (Fig. 3b), which provides evidence for longer range magnetic ordering of these magnetic NPs. Superconducting quantum interference device (SQUID) measurements have been attempted without success due to the insufficient amount of nanodeposits present.

Conclusion

Uniformly distributed cubic Fe NPs with an average side length of 56 nm and a narrow size distribution were deposited potentiostatically by amperometry from an $FeCl_2$ and H_3BO_3 solution onto a H-Si(100) substrate. XPS analysis shows that the individual NPs consist of a substantial Fe core and a thin Fe_2O_3 shell (2.5 nm thick), while the corresponding GIXRD data indicate the crystal structure of the Fe core to be bcc. Given the relatively large amount of the Fe core compared to the Fe_2O_3 shell, and that bcc Fe is known to be ferromagnetic, our MFM measurements reveal some of the interesting magnetic properties of these cubic Fe core-shell NPs.

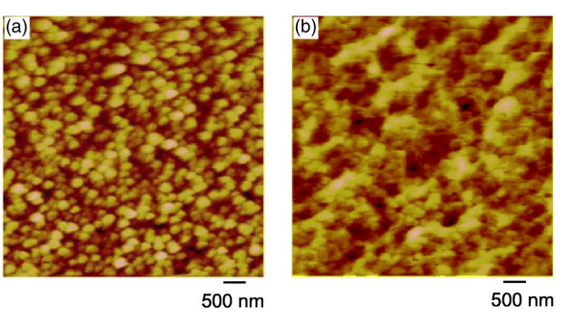

Figure 3. (Color online) (a) Tapping-mode AFM and (b) MFM images of Fe cuboidal nanoparticles deposited on H-terminated Si(100). The MFM image was obtained at a lift distance of 50 nm interleaved with the scans that build up the AFM image.

Acknowledgments

This work was supported by the Natural Sciences and Engineering Research Council of Canada. We are indebted to Dr. Roman Engel-Herbert and Dr. Thorsten Hesjedal for helpful discussions.

References

1. J. F. Bobo, L. Gabillet, and M. Bibes, *J. Phys.: Condens. Matter*, **16**, S471 (2004).
2. S. Sun, C. B. Murray, D. Weller, L. Folks, and A. Moser, *Science*, **287**, 1989 (2000).
3. P. Tartaj, M. P. Morales, S. Veintemillas-Verdaguer, T. González-Carreño, and C. J. Serna, *J. Phys. D*, **36**, R182 (2003).
4. Y. G. Sun and Y. N. Xia, *Science*, **298**, 2176 (2002).
5. H. R. Zhang, C. M. Shen, S. T. Chen, Z. C. Xu, F. S. Liu, J. Q. Li, and H. J. Gao, *Nanotechnology*, **16**, 267 (2005).
6. S. Gangopadhyay, G. C. Hadjipanayis, S. I. Shah, C. M. Sorensen, K. J. Klabunde, V. Papaefthymiou, and A. Kostikas, *J. Appl. Phys.*, **70**, 5888 (1991).
7. H. A. Hosein, D. R. Strongin, M. Allen, and T. Douglas, *Langmuir*, **20**, 10283 (2004).
8. Y. Q. Li, P. Xiong, S. von Molnár, S. Wirth, Y. Ohno, and H. Ohno, *Appl. Phys. Lett.*, **80**, 4644 (2002).
9. A. D. Kent, T. M. Shaw, S. von Molnár, and D. D. Awschalom, *Science*, **262**, 1249 (1993).
10. M. A. McCord and D. D. Awschalom, *Appl. Phys. Lett.*, **57**, 2153 (1990).
11. S. Jain, S. Y. Chan, A. O. Adeyeye, and C. B. Boothroyd, *Int. J. Nanosci.*, **3**, 631 (2004).
12. F. Zavaliche, W. Wulfhekel, H. Xu, and J. Kirchner, *J. Appl. Phys.*, **88**, 5289 (2000).
13. R. Kläsges, C. Carbone, W. Eberhardt, C. Pampuch, O. Rader, T. Kachel, and W. Gudat, *Phys. Rev. B*, **56**, 10801 (1997).
14. D. P. Adams, T. M. Mayer, and B. S. Swartzentruber, *Appl. Phys. Lett.*, **68**, 2210 (1996).
15. A. Butera, J. L. Weston, and J. A. Barnard, *IEEE Trans. Magn.*, **34**, 1024 (1998).
16. J. M. Gallego and R. Miranda, *J. Appl. Phys.*, **69**, 1377 (1991).
17. J. D. Lee, K. H. Kim, J. J. Lee, S. Y. Jeong, B. Y. Ahn, H. S. Kim, and Y. W. Shin, *Jpn. J. Appl. Phys., Part 1*, **45**, 2470 (2006).
18. J. Zarpellon, H. F. Jurca, J. J. Klein, W. H. Schreiner, N. Mattoso, and D. H. Mosca, *J. Electrochem. Soc.*, **152**, C808 (2005).
19. H. Matsushima, Y. Fukunaka, Y. Ito, A. Bund, and W. Plieth, *J. Electroanal. Chem.*, **587**, 93 (2006).
20. L. Y. Zhao, K. R. Eldridge, K. Sukhija, H. Jalili, N. F. Heinig, and K. T. Leung, *Appl. Phys. Lett.*, **88**, 033111 (2006).
21. M. Schlesinger and M. Paunovic, *Modern Electroplating*, 4th ed., p. 461, Wiley, New York (2000).
22. *Handbook of Semiconductor Wafer Cleaning Technology*, W. Kern, Editor, Noyes, Park Ridge, NJ (1993).
23. E. Sacher and N. S. McIntyre, *Phys. Rev. B*, **33**, 2845 (1986).
24. M. C. Biesinger, C. Brown, J. R. Mycroft, R. D. Davidson, and N. S. McIntyre, *Surf. Interface Anal.*, **36**, 1550 (2004), and references therein.
25. J. V. Zoval, R. M. Stiger, P. R. Biernacki, and R. M. Penner, *J. Phys. Chem.*, **100**, 837 (1996).
26. F. J. Himpsel, B. S. Meyerson, F. R. McFeely, J. F. Morar, A. Taleb-Ibrahimi, and J. A. Yarmoff, in *Photoemission and Absorption Spectroscopy of Solids and Interfaces with Synchrotron Radiation*, M. Campagna and R. Rosei, Editors, p. 203, North-Holland, Amsterdam (1990).
27. H. T. Johnson-Steigelman, A. V. Brinck, S. S. Parihar, and P. F. Lyman, *Phys. Rev. B*, **69**, 235322 (2004).
28. M. C. Porté-Durrieu, C. Labrugère, F. Villars, F. Lefebvre, S. Dutoya, A. Guette, L. Bordenave, and C. Baquey, *J. Biomed. Mater. Res.*, **46**, 368 (1999).
29. R. Alfonsetti, G. De Simone, L. Lozzi, M. Passacantando, P. Picozzi, and S. Santucci, *Surf. Interface Anal.*, **22**, 89 (1994).
30. J. F. Moulder, W. F. Stickle, P. E. Sobol, and K. D. Bomben, in *Handbook of X-Ray Photoelectron Spectroscopy*, 2nd ed., J. Chastain, Editor, Perkin-Elmer Corp., Eden Prairie, MN (1992).
31. C. Pulgarin and J. Kiwi, *Langmuir*, **11**, 519 (1995).
32. T. Choudhury, S. O. Saied, J. L. Sullivan, and A. M. Abbot, *J. Phys. D*, **22**, 1185 (1989).
33. D. Briggs and M. P. Seah, *Practical Surface Analysis*, Vol. 1, 2nd ed., Wiley, New York (1990).
34. B. O. Cho, J. P. Chang, J. H. Min, S. H. Moon, Y. W. Kim, and I. Levin, *J. Appl. Phys.*, **93**, 745 (2003).
35. B. D. Cullity, *Elements of X-Ray Diffraction*, Addison-Wesley, Reading, MA (1978).